1 **Experimental evidence for abiotic formation of low-temperature proto-dolomite**

2 **facilitated by clay minerals**

3

4 Deng Liu[1, 2, *], Yangyang Xu[1], Dominic Papineau[1, 3, 4, 5], Na Yu[2], Qigao Fan[2], Xuan

5 Qiu[1] and Hongmei Wang[1, 2, *]

6

7 [1]State Key Laboratory of Biogeology and Environmental Geology, China University of

8 Geosciences, Wuhan 430074, China

9 [2]School of Environmental Studies, China University of Geosciences, Wuhan 430074,

10 China

11 [3]London Centre for nanotechnology, University College London, 17-19 Gordon

12 Street, London, UK

13 [4]Department of Earth Sciences, University College London, London, UK

14 [5]Center for Planetary Sciences, University College London, London, UK

15

16 Corresponding authors:

17 Deng Liu (liud_cug@126.com) and Hongmei Wang (wanghmei04@163.com)

18

19 Further revised for *Geochimica et Cosmochimica Acta*

20

21 December 21, 2018

22

ABSTRACT

The origin of sedimentary dolomite is a subject of long-standing enigma that still awaits resolution. Previous studies have shown that room temperature synthesis of abiotic dolomite is rarely achieved and primary (proto-)dolomite precipitation is closely associated with microbial activities. In this study, we demonstrate through laboratory carbonation experiments that highly negative-charged clay minerals (as indicated by the values of zetal potential) such as illite and montmorillonitecan aid the precipitation of abiotic proto-dolomite under ambient conditions, whereas nearly-neutral charged kaolinite exerts negligible influence on such process. In comparison to montmorillonite, illite has higher surface-charge density, thus is more effective in catalyzing proto-dolomite precipitation. Furthermore, the signal of proto-dolomite in carbonate neoformations is enhanced with increasing concentrations of illite or montmorillonite. On the basis of these results, we suggest that clay minerals catalyze dolomite formation perhaps via electrostatic binding of Mg^{2+} and Ca^{2+} ions and simultaneously desolvating these strongly hydrated cations, a crucial step for dolomite crystallization. The resulting proto-dolomites display the morphologies, textures, and structures similar to those of biogenic dolomite reported before, which are considered precursors of ordered sedimentary dolomite. Therefore, our results offer a possible route to authigenic dolomite found in sedimentary environments.

1. INTRODUCTION

Dolomite [CaMg(CO$_3$)$_2$] is an important mineral component of sedimentary rocks (Warren, 2000). In pre-Holocene geological records, massive amount of dolomite formation could be commonly found in the carbonate paltforms (Given and Wilkinson, 1987; Burns et al., 2000; Warren, 2000). Most ancient dolostone rocks which contain more than >75% dolomite by volume are even hundreds to thousands meter thick and cover areas of hundreds of kilometers wide (Warren, 2000; McKenzie and Vasconcelos, 2009). By contrast, the recent occurrences of dolomite are extremely rare in marine sediments, despite the fact that modern seawater is thermodynamically oversaturated with respect to this mineral (Burns et al., 2000). Such apparent discrepancy has stimulated intense studies and debates regarding the genesis of dolomite.

Most geologists contend that the majority of ancient dolomites (massive dolostone in particular) formed as a diagenetic replacement of limestone (i.e, dolomitization: $2CaCO_3 + Mg^{2+} \rightarrow CaMg(CO_3)_2 + Ca^{2+}$ or $CaCO_3 + Mg^{2+} + CO_3^{2-} \rightarrow CaMg(CO_3)_2$) (e.g., Land, 1985; Given and Wilkinson, 1987; Budd, 1997; Machel, 2004). This hypothesis has been supported by the geological observations (e.g., poor preservation of fossils, coarse dolomite grains with dissolution pores and cavities) in dolostone and reinforced by the fact that laboratory synthesis of dolomite is difficultly achieved at Earth surface temperatures (<60 °C), whereas it is relatively uncomplicated and proceeds at a rapid rate under higher temperature diagenetic conditions (Land, 1980, 1998; Morrow, 1982; Sibley et al., 1987; Arvidson and Mackenzie, 1999; Kaczmarek and Thornton, 2017). Furthermore, thermal dolomitization experiments have indicated

3

that metastable precursors exclusively occur at the expense of calcite (or aragonite)

above 100 °C and finally convert to ordered-dolomite at temperature over 150 °C (e.g.,

Graf and Goldsmith, 1956; Baker and Kastner, 1981; Sibley et al., 1994; Kaczmarek

and Sibley, 2011; Jonas et al., 2017). These metastable phases include proto-dolomite

(sometimes referred to as "disordered-dolomite" or "very high-magnesium calcite,

VHMC") and calcian dolomite. Compared to their highly ordered counterpart (i.e.,

ordered-dolomite or stoichiometric dolomite), proto-dolomite displays none or very

weak cation ordering and calcian dolomite exhibits partly ordered crystal structures,

despite both of these Ca-Mg carbonates having compositions close to ordered-dolomite

(Gregg et al., 2015).

In spite of their paucity, the Holocene dolomites have been repeatedly observed in

evaporitic environments worldwide (Wells, 1962; Middelburg et al., 1990; Vasconcelos

and McKenzie, 1997; Wright, 1999; van Lith et al., 2002; Wright and Wacey, 2005;

Bontognali et al., 2010, 2012; Deng et al., 2010; Meister et al., 2011; Brauchli et al.,

2016). Interestingly, these dolomites have been demonstrated to be low-temperature

primary (or at least very early diagenetic) dolomite that directly precipitates from

saturated solutions ($Ca^{2+} + Mg^{2+} + 2CO_3^{2-} \rightarrow CaMg(CO_3)_2$) (McKenzie and

Vasconcelos, 2009; Petrash et al., 2017). In addition, Holocene dolomites typically

precipitate as proto-dolomite and calcian dolomite in the upper sediments, while they

occur as more stoichiometric dolomite rhombs in the deeper layers, suggesting the

recrystallization of dolomite upon burial diagenesis (Gregg et al., 1992; Vasconcelos

and McKenzie, 1997; Wright, 1999; Petrash et al., 2017). Several dolomite-forming

environments, such as sabkhas of United Arab Emirates (UAE) and Coorong Lagoon

of the South Australia, have been proposed as analogs for the origin of ancient

dolomites (McKenzie and Vasconcelos, 2009). Besides the favorable abiotic

geochemical parameters (e.g., oversaturated state, high Mg/Ca ratio and salinity), there

may be natural catalysts overcoming the kinetic barriers to low-temperature dolomite

formation. In fact, sulfate-reducing bacteria (Vasconcelos et al., 1995; Vasconcelos and

McKenzie, 1997; Wright, 1999; Wright and Wacey, 2005; Deng et al., 2010; Bontognali

et al., 2012; Krause et al., 2012), methanogenic archaea (Roberts et al., 2004; Kenward

et al., 2009), fermenting bacteria (Zhang et al., 2015) and various aerobic halophiles

(Rivadeneyra et al., 2000, 2006; Sánchez-Román et al., 2008, 2009, 2011a, 2011b;

Deng et al., 2010; Balci and Demirel, 2016; Disi et al., 2017; Qiu et al., 2017) have

been identified as effective catalysts that promote dolomite nucleation and growth.

Proposed catalytic functions for microorganisms in dolomite formation include

increasing dolomite saturation state and, providing cell walls and organic secretions

(e.g., exopolymeric substances) serving as template for dolomite crystallization

(McKenzie and Vasconcelos, 2009; Zhang et al., 2012a, 2015; Kenward et al., 2013;

Roberts et al., 2013; Bontognali et al., 2014a; Qiu et al., 2017). Noticeably, an argument

is recently proposed by Gregg and co-workers who reevaluated the published XRD data

of biogenic dolomites and found that these precipitates are proto-dolomite (or VHMC)

rather than presumably reported ordered-dolomite (Gregg et al., 2015). Nevertheless,

as stated earlier, proto-dolomite is considered an important precursor for ordered-

dolomite in sediments and sedimentary rocks. As such, a two-stage process, which

111   begins with proto-dolomite precipitation by means of nature catalysts (e.g., microbes)

112   and is followed by diagenesis-controlled recrystallization of proto-dolomite towards

113   ordered-dolomite, could account for the occurrence of Holocene dolomites and was

114   probably involved in the formation of ancient dolomites.

115   In contrast to the growing body of research on microbe-catalyzed dolomite

116   formation, the role of naturally-occurring abiotic mineral catalysts has been largely

117   overlooked. Clay minerals are ubiquitous on the Earth's surface and they are the

118   important mineral constituents of aquatic sediments (Chamley, 1989). Although there

119   are a few studies concerning the effect of clay minerals on abiotic dolomite formation,

120   the interpretations are largely contradictory. Specifically, based on petrographic and

121   mineralogic investigations, some suggest a close relationship between the clay minerals

122   and abiotic dolomite formation in several depositional settings, such as dolostones

123   (Kahle, 1965; Botha and Huges, 1992; Wanas and Sallam, 2016), cave speleothems

124   (Pérez et al., 2015) and soils (Capo et al., 2000; Casado et al., 2014; Cuadros et al.,

125   2016; Díaz-hernández et al., 2018). In these studies, clay minerals were proposed to be

126   a source of magnesium for dolomite formation and/or function as nucleation centers for

127   dolomite crystals (e.g., Kahle, 1965; Wanas and Sallam, 2016). However, no

128   relationship between these two types of mineral has been detected in other sedimentary

129   environments (Hatfield and Rohrbacker, 1966; Lumsden, 1974). Therefore, laboratory

130   experiments are required to explicitly probe whether clay minerals can facilitate abiotic

131   (proto-)dolomite precipitation. This interaction could arise from negative charges on

132   the surface of clay minerals, which is analogous to that of microbes, and thus serve as

133   a template for (proto-)dolomite nucleation.

134   To test the aforementioned hypothesis, we performed a series of lab-bench

135   carbonation experiments using different clay minerals at room temperature. Our results

136   show that negatively-charged clay minerals can accelerate the abiotic precipitation of

137   proto-dolomite under ambient conditions and this catalytic effect might depend on their

138   charge densities.

139

140   **2. MATERIALS AND METHODS**

141   **2.1. Clay mineral preparation and analyses**

142   Illite (IMt-1), montmorillonite (SWy-2) and kaolinite (KGa-1b) were selected for

143   the experiments. The criteria for the mineral selection are based on their ubiquitous

144   occurrence in sediments and the various magnitude of charge density on their layer

145   surface. Both illite and montmorillonite belong to the 2:1 layer-type clay mineral that

146   consists of an octahedral sheet sandwiched between two tetrahedral sheets, whereas

147   kaolinite possesses a 1:1 dioctahedral structure (Chamley, 1989). Specifically for most

148   2:1 layered clay minerals (e.g., illite and montmorillonite used in this study), their

149   tetrahedrally-coordinated Si(IV) and octahedral Al(III) are partially replaced by lower

150   valency cations, resulting in a net negative surface charge. By contrast, kaolinite is

151   much less substituted by foreign cations, thus displaying negligible surface charge

152   (Chamley, 1989).

153   All clay minerals used were purchased from the Source Clays Repository of the

154   Clay Minerals Society (West Lafayette, Indiana, USA). Preparation of each clay sample

155 consisted in manual milling in a mortar followed by sieve through a 200-mesh stainless

156 steel sieve (0.074 mm). The fraction with size less than 200-mesh was then washed

157 three times with doubly distilled water (ddH$_2$O), collected, and then air-dried for all

158 experiments. The detailed information regarding the physical and chemical properties

159 is summarized in Table 1.

160   The surface electronic property of clay minerals was characterized by zeta

161 potential (ξ) measurements. Briefly, the samples were suspended in ddH$_2$O (pH=7.0) at

162 a concentration of 2 g/L. Upon homogeneous dispersion, clay suspensions were

163 transferred into an electrophoretic cell, and the ξ value of clay minerals was measured

164 using a Zeta potential analyzer (ZetaSizer Nano ZS, Malvern Instruments, UK). It is

165 well known that the negative electric charge of clay minerals is mainly attributed to

166 their edge-surface hydroxyl groups (Chamley, 1989). As such, thermogravimetric

167 analysis (TGA) was performed to determine the amount of surface-bound hydroxyl in

168 used clay minerals. TGA analyses were made on a TGA system (Netzsch STA449F3,

169 Germany). These analyses were performed on pre-weighted samples of about 20 mg

170 heated in a corundum crucible from 30 to 1000 °C at a heating rate of 5 °C min^{-1} under

171 N$_2$ atmosphere.

172 **2.2. Abiotic syntheses of carbonate minerals and chemical analyses**

173   A precipitate solution with a Mg/Ca molar ratio of 8 was prepared for carbonation

174 experiments. This Mg/Ca value is higher than that of present sweater (~5.2), but lies

175 within the range of values measured in dolomite-forming environments (Deng et al.,

176 2010). The precipitation system consisted of 10 mM CaCl$_2$, 80 mM MgCl$_2$·6H$_2$O, 20

177   mM Na_2CO_3, and different concentrations of clay minerals (0, 1, 2, 4 and 6 g/L;

178   corresponding to different amounts of surface charge available for interacting with Ca^{2+}

179   and Mg^{2+} ions).

180   In brief, aqueous solutions of $CaCl_2/MgCl_2·6H_2O$ and of Na_2CO_3 were first

181   prepared as stock solutions. Different amounts of clay minerals were added into

182   aforementioned Ca^{2+}/Mg^{2+} solution. After being stirred at room temperature overnight,

183   the pH of mixture was adjusted to 7.0 by using 0.1 M NaOH. Then the solution of

184   Na_2CO_3 was added dropwise into the clay suspension, leading to form gel-like

185   precipitate. After about 30 min, the gel was placed in an incubator at 30 °C and all

186   synthetic experiments reported are performed in duplicate.

187   Solution pH, aqueous Ca^{2+} and Mg^{2+} as well as dissolved inorganic carbon (DIC)

188   were measured immediately after solutions were mixed (i.e., in the initial carbonation

189   stage) and after 30-day ageing. The pH was determined using a Denver UB-7 meter

190   (Denver, USA) with an uncertainty of ± 0.01 pH units. The concentrations of Ca^{2+} and

191   Mg^{2+} were analyzed by inductively coupled plasma-optical emission spectrometry

192   (ICP-OES, Thermofisher ICAP6300, USA). Determination of DIC was performed by

193   using Shimadzu SCN analyzer (TOC-V, Shimadzu, Japan). The concentrations of

194   CO_3^{2-} were further calculated from measured pH and DIC. On the basis of above

195   analyses, the saturation indices (SI) with respect to common carbonates (calcite,

196   aragonite, monohydrocalcite and proto-dolomite) could be calculated using PHREEQC

197   (version 2; Parkhurst and Appelo, 1999).

198   **2.3. Preparation of mineral standards**

199   Hydromagnesite can easily be misidentified as dolomite (Zhang et al., 2012a),

200 because the (310) peak of hydromagnesite appears at 30.818° (2θ, Cu Kα), very close

201 to the strongest (104) reflection of (proto-)dolomite. To avoid this possible

202 misidentification, a hydromagnesite, together with hydrothermally-synthesized proto-

203 and ordered-dolomites, was prepared as a reliable standard for inferring the

204 mineralogical composition of carbonate neoformations. Hydromagnesite, originally

205 collected from hypersaline lakes on the Tibetan Plateau, was acquired from Xibeili

206 mineral company (Jiangsu, China). Proto- and ordered-dolomite standards were

207 prepared at 80 °C and 200 °C, respectively, based on the method of Rodriguez-Blanco

208 et al. (2015).

209 **2.4. Crystal characterization**

210   After one month, the resulting precipitates were obtained by centrifugation, and

211 subsequently rinsed three times with ddH$_2$O, and then air-dried. Multiple methods were

212 used for mineral analysis, including X-ray diffraction (XRD), Raman spectroscopy, and

213 scanning and transmission electron microscopy (SEM and TEM).

214   The samples were analyzed with a Bruker D8 Advance XRD using Cu Kα

215 radiation. The operation voltage and current maintained at 40 kV and 40 mA,

216 respectively. The samples were scanned from 3 to 65° 2θ stepping at 0.02° with a count

217 time of 1 s per step. The MgCO$_3$ molar fraction in the crystal lattice of Ca-Mg

218 carbonates was calculated from *d*-spacing of (104) peak using the empirical curve

219 developed by Bischoff et al. (1983). Solids produced in the reactor with 6 g/L illite IMt-

220 1, along with pristine IMt-1 and aforementioned mineral standards, were analyzed by

221 Raman spectroscopy. The Raman spectra were acquired using a Renishaw RM-1000

222 laser Raman microscope system in the range between 100 and 1200 cm^{-1} at an interval

223 of 1 cm^{-1}. A 514.5 nm Ar$^+$ laser was used as the excitation source. Spectral peak

224 positions were calibrated using the 520.5 cm^{-1} line of silicon as a standard. The dried

225 solid samples were Pt-coated prior to observation using a Hitachi SU8010 SEM. In

226 addition, a Horiba EX-350 energy-dispersive X-ray spectrometer (EDS) was employed

227 in the SEM to determine the elemental composition of the solid experimental products.

228 The SEM was operated at an accelerating voltage of 5-15 kV. TEM observations and

229 EDS analyses were performed with an FEI Talos F200X TEM with an accelerating

230 voltage of 200 kV. Samples for TEM analyses were first dispersed in ethanol and then

231 pipetted onto 300 mesh copper TEM grids with a nitrocellulose membrane and carbon

232 coating.

233

234 **3. RESULTS**

235 **3.1. Characterization of clay samples**

236   XRD results of pristine clay samples in the size range of less than 200 mesh reveal

237 that both illite IMt-1 and montmorillonite SWy-2 also contain trace amounts of quartz,

238 while kaolinite KGa-1b is highly pure (Table 1). The zeta potential of the clay minerals

239 varies significantly. Specifically, the ξ value is -41.99 mV for illite, -34.51 mV for

240 montmorillonite, and -3.93 mV for kaolinite, which indicates that illite and

241 montmorillonite have much higher layer-charge density than kaolinite. These results

242 are consistent with the conventional view that illite and montmorillonite are 2:1 layer

clay minerals that carry a net negative electric charge that results from extensive

isomorphous substitution of cations in their lattice structures, but 1:1 layer type

kaolinite is nearly-neutral charged (Chamley, 1989). TGA results can also be used to

compare the amount of surface hydroxyl between illite and montmorillonite. Two

significant weight loss steps are observed in these clays: a dehydration first stage

followed by a dehydroxylation second stage (Fig. S1). Results show that weight losses

from dehydroxylation are 6.1% and 3.6% for illite and montmorillonite respectively,

which confirms that illite has significantly more hydroxyl than montmorillonite (Fig.

S1).

3.2. Changes of aqueous chemistry as a result of carbonation

As shown in Table 2, the ionic compositions of the reactors with 6 g/L clay

minerals are selected as representatives to investigate the geochemical changes upon

carbonation. In general, the pH of each solution decreases by ca. 0.7 pH units at the end

of experiments, which is ascribed to the decline in CO_3^{2-} concentrations. As a result of

carbonate precipitation, Ca^{2+} ions for each reactor are largely depleted. Even though

the precipitation solutions are oversaturated with respect to Mg-bearing carbonates (e.g.,

proto-dolomite), a significant decrease of Mg^{2+} is only observed in the systems with

illite or montmorillonite, indicating that various carbonates occur in the clay-amended

reactors.

3.3. Characterization of neoformed Ca-Mg carbonates

3.3.1. XRD results

264   As representatives, the XRD patterns of the particles grown in the presence of 6

265   g/L clay minerals are presented in Figs. 1 and 2. Without clay minerals, only aragonite

266   is obtained (Figs. 1A). When clay minerals are introduced into the reactors, the solid

267   products change greatly. Specifically, in the illite-amended system, dolomite-like

268   material is the only carbonate phase detected (Fig. 1). In comparison, the characteristic

269   peaks [(011), (100) and (-110)] of hydromagnesite are absent from our experiments

270   (Fig. 1), which suggests that this carbonate phase is dolomite rather than

271   hydromagnesite. The (104) reflection position of our produced dolomite is around

272   30.735° 2θ (d_{104}=0.2907 nm). This value reveals that its $MgCO_3$ content is ~46.2 mol%

273   (Bischoff et al., 1983), much close to the stoichiometric composition. To assess the

274   degree of cation ordering of low-temperature dolomite, the XRD patterns of illite-

275   assisted dolomite, proto- and ordered-dolomite standards are further compared. It can

276   be seen that the XRD pattern of illite-assisted carbonate precipitate is quite similar to

277   that of proto-dolomite, as evidenced by the lack of superstructure ordering peaks [e.g.,

278   (101), (015) and (021)] and broad nature of the reflections (Fig. 1). It has been suggested

279   that poor cation ordering and structural water could account for these characteristic

280   appearances of the XRD pattern of proto-dolomite (Kelleher and Redfern, 2002). Not

281   limited to the system with illite, proto-dolomite, accompanying with trace aragonite, is

282   also observed in the montmorillonite-amended reactor (Fig. 2). However, its reflection

283   intensity is significantly lower. By contrast, instead of proto-dolomite, only weak XRD

284   signals characteristic of monohydrocalcite are detected in carbonate products from

285   kaolinite-assisted experiments (Fig. 2). The XRD results show that low-temperature

286   formation of proto-dolomite can be catalyzed by clay minerals and thus suggest that

287   this process may be mediated by negatively charged surfaces; that is, illite with highest

288   charge density represents the most positive effective on proto-dolomite precipitation,

289   and lower-charged montmorillonite contributes less to this reaction, while nearly-

290   neutral charged kaolinite has a negligible impact.

291   In order to elucidate the relationship between the charge of clay minerals and the

292   formation of proto-dolomite, the effect of clay concentration (i.e., charge magnitude in

293   reactors) on proto-dolomite precipitation is also evaluated (Figs. S2 and S3). As

294   expected, the peak intensity of the (104) plane of proto-dolomite also progressively

295   increases with increasing concentrations of illite (Fig. S2) or montmorillonite (Fig. S3).

296   In addition, aragonite and monohydrocalcite can also be precipitated in

297   montmorillonite-amended experiments (Fig. S3) and when low concentration of illite

298   is used (Fig. S2).

299   **3.3.2. Raman data**

300   As an independent characterization of the crystal structure of the experimentally-

301   produced phase, the Raman spectra of carbonate precipitate with 6 g/L illite are directly

302   compared to those of illite, and standards of proto-dolomite, ordered-dolomite, and

303   hydromagnesite. Typically for dolomite, there four distinct vibrational modes can be

304   observed in the range of 100-1200 cm^{-1} (Fig. 3). In general, compared to ordered-

305   dolomite, proto-dolomite exhibits a broader peak width and band positions slightly

306   shifted to lower wavenumbers, from 1097 to 1095 cm^{-1}. Unlike dolomite,

307   hydromagnesite only displays two characteristic modes (Fig. 3). After carbonation,

308   there is one distinct band and three small humps emerged in illite samples (Fig. 3). In

309   comparison to the standards, the position of these new peaks is similar to that of proto-

310   dolomite, which independently confirms the existence of proto-dolomite in illite-

311   amended carbonation experiments.

312   **3.3.3. SEM observations**

313   SEM images show that proto-dolomite crystals are exclusively distributed on the

314   edge of platy illite particles, which suggests that the edges rather than basal surfaces

315   are more effective catalytic sites for proto-dolomite crystallization (Fig. 4). These

316   proto-dolomite crystals are 1-3 μm in size, and are either randomly dispersed on small

317   illite particles (Fig. 4A) or in the form of aggregates covering the large illite crystals

318   (Figs. 4B and C). High-magnification images of proto-dolomite crystals reveal a

319   cauliflower-like (Fig. 4D) or dumbbell-shaped (Fig. 4E) structures. Nanoscale-

320   resolution images show that the proto-dolomite has a granular texture comprised of

321   many spherical crystallites around 10-20 nm in size (Fig. 4F). Elemental mapping by

322   EDS reveals striking differences between illite and neoformed proto-dolomite (Figs.

323   4G-J). The proto-dolomite particles have high level of homogenously distributed Ca

324   and Mg, but a trace amount of Si, while the signals of Ca and Mg are nearly invisible

325   on the surface of Si-rich illite crystals (Figs. 4H-J). The chemical compositions of illite

326   and proto-dolomite are further obtained by EDS spot scan, as shown in Figs. 4K-L. In

327   comparison to illite, proto-dolomite particle is rich in C, O, Mg and Ca, and displays

328   similar Mg and Ca contents (Mg-Kα and Ca-Kα). Proto-dolomite in the reactor with

329   montmorillonite exhibits only spheroidal morphology (Figs. 5A and B), and is

surrounded by flaky-shaped montmorillonite (see Fig. 5B). The $MgCO_3$ content of

these spheroids reaches approximately 47 mol% as determined by EDS (Fig. 5C). High

magnification images show that dolomite spheroids are also composed of numerous

nanoparticles (Fig. 5D), similar to those obtained in illite systems. Furthermore, SEM-

EDS results indicate that dendritic-shaped aragonite is also produced in the presence of

montmorillonite (Fig. S4).

3.3.4. TEM observations

The occurrence of proto-dolomite is also validated by TEM investigation. The

TEM photographs of a representative sample from the 6 g/L illite system are presented

in Fig. 6. In agreement with the SEM results, micron-sized proto-dolomites are

primarily located on the illite external surfaces and have a spheroidal or fan

(cauliflower)-like shape (Fig. 6A). The $MgCO_3$ content in the proto-dolomite is

calculated to be ca. 46 mol% from the TEM-EDS data, again consistent with

aforementioned SEM-EDS measurements. High-resolution TEM (HRTEM) images

further confirm that the proto-dolomite crystals are made of numerous, randomly

distributed, 10-30 nm sized nanoscopic crystals (Figs. 6B and C). The selected-area

electron diffraction (SAED) pattern of these nanoparticles shows diffraction rings

matching (hkl) indices of (012), (104), (006) and (113) of dolomite (Fig. 6C). However,

the super-lattice reflections [e.g., (015), (101) and (021)] indicating the cation ordering

are not found, which again independently confirms that proto-dolomite is synthesized

in these experiments and agrees with our XRD and Raman spectra. The crystal lattice

fringes also demonstrate the presence of proto-dolomite with a 2.906 Å d-spacing that

corresponds to the (104) plane of proto-dolomite and by its two sets of {104} face with

angle of 75° (Fig. 6D).

4. DISCUSSION

4.1. The possible role of clay minerals in proto-dolomite crystallization

According to previous reports, the intrinsic difficulty to precipitate both proto- and ordered-dolomite is attributed to the Mg-hydration effect (e.g., Lippmann, 1982; de Leeuw and Parker, 2001; Romanek et al., 2009). In general and similarly to Ca^{2+} ions, Mg^{2+} ions are bound to water molecules, thus forming metal-H_2O association in aqueous solutions (Lippmann, 1973, 1982; Romanek et al., 2009; Hamm et al., 2010). Previous experimental and computational studies have demonstrated that the water coordination number for Mg^{2+} (6.0) is smaller than that for Ca^{2+} (6.0-9.2, with the mean number of 7.3) (Jalilehvand et al., 2001; Jiao et al., 2006; Hamm et al., 2010). However, as compared to Ca^{2+}, much more energy is required to shed the water molecules around Mg^{2+} (1926 kJ/mole for Mg^{2+} vs. 1579 kJ/mole for Ca^{2+}), arising from the strong outer solvation shell of Mg^{2+} (Lippmann, 1973; Hamm et al., 2010). As a consequence, the persistent hydration shell of Mg^{2+} can poison the growth of Ca-Mg carbonates such that the formation of Mg-free aragonite is favored when Mg:Ca molar ratio exceeds 4:1 (Falini et al., 1996; Lenders et al., 2012; Zhang et al., 2012b; Shen et al., 2014, 2015). As such, the predominance of aragonite over calcite and Ca-Mg carbonates takes place in modern seawater which has an average Mg/Ca molar ratio of ~5.2, and it is also observed in our clay-free systems with a Mg/Ca molar ratio of 8 (Fig. 1A).

374   However, it is generally considered that this Mg^{2+}-H_2O association can be

375   destabilized by changing some physicochemical parameters. For instance, increase in

376   salinity might reduce water activity and subsequently decrease the hydration energy of

377   Mg (van Lith et al., 2002). Furthermore, dehydration of Mg^{2+} and subsequent Mg

378   incorporation into growing Ca-Mg carbonates can also take place in the presence of

379   microorganisms, microbial exudates or other organo-molecules, leading to

380   crystallization of magnesian calcite (e.g., Falini et al., 1996; De Yoreo and Dove, 2004;

381   Rivadeneyra et al., 2004; Stephenson et al., 2008; González-Muñoz et al., 2010;

382   Lenders et al., 2012; Han et al., 2013) and even (proto-)dolomite (e.g., Vasconcelos et

383   al., 1995; Roberts et al., 2004, 2013; Sánchez-Román et al., 2008; Bontognali et al.,

384   2012, 2014a; Zhang et al., 2012a, 2015). Moreover, carboxyl moiety (R-COO⁻)

385   associated with microbes and organo-molecules have been identified as the crucial

386   functional group facilitating the loading of Ca^{2+} and Mg^{2+} during Ca-Mg carbonate

387   growth (Kenward et al., 2013; Qiu et al., 2017).

388   There are at least two distinct hypotheses proposed to explain the positive role of

389   microbes and organo-molecules in dewatering of Mg^{2+}-H_2O complexes: (1) a metal-

390   chelation model (Mirsal and Zankl, 1985; Romanek et al., 2009; Wang et al., 2009;

391   Kenward et al., 2013; Roberts et al., 2013) and (2) an adsorption-displacement

392   mechanism (Zhang et al., 2015). In the first model, it has suggested that electronegative

393   carboxyl functional groups can bind and partially dewater Mg^{2+}-H_2O complexes,

394   generating Mg^{2+}-carboxyl group complexes. In doing so, Mg^{2+}-carboxyl complex

395   requires much lower energy for carbonation than Mg^{2+}-H_2O complex (Kenward et al.,

396 2013; Roberts et al., 2013). In the adsorption-displacement mechanism, microbial

397 exopolymers are preferentially adsorbed onto the growing Ca-Mg carbonate surface

398 replacing the surface water molecules, which would otherwise be associated with Mg^{2+},

399 thereby benefiting the diffusion of Mg^{2+} into crystal structure (Zhang et al., 2015).

400   Our experiments demonstrate that clay minerals can also facilitate and expedite

401 proto-dolomite precipitation. Several lines of evidence suggest that clay mineral-

402 mediated proto-dolomite formation might proceed through a metal-chelation

403 mechanism. First as solid phases, clay minerals apparently cannot work in the same

404 way as soluble microbial secretions (e.g., extracellular exopolymers, carboxylic acids

405 and others), which could be easily adsorbed to growing carbonate as mentioned above.

406 Second, it appears that only clay minerals with negative charges such as illite and

407 montmorillonite promote proto-dolomite formation, which suggests that these clay

408 minerals perhaps serve a function similar to that of negatively-charged microbial cells

409 via binding Mg and Ca ions, thus facilitating the dehydration of Mg and Ca. Third, in

410 comparison to montmorillonite, illite has a greater surface charge density (as evidenced

411 by ξ values), and therefore is shown to be more efficient at enhancing dolomite

412 precipitation, further indicating that the magnitude of charge density plays a

413 fundamental role in dolomite formation. Such hypothesis is reinforced by the

414 observations that the proto-dolomite signal in XRD is enhanced with increasing

415 concentrations of illite or montmorillonite (corresponding to elevated charge density in

416 precipitation reactor). A similar finding has been reported by Kenward and co-workers

417 who demonstrated that the formation of (proto-)dolomite can be achieved in the

418 presence of microorganisms with high charge density (Kenward et al., 2013).

419 Fourth, clay minerals are negatively charged primarily due to a large number of edge-

420 bound hydroxyl groups. If clay minerals catalyze proto-dolomite crystallization via

421 their surface binding, proto-dolomite should be preferably formed on the edge surface

422 of clay particles. Since montmorillonite is irregular in shape, it is difficult to distinguish

423 between its edge surface and basal surface under SEM. However, this is not a problem

424 for illite. Our SEM results reveal that newly-formed proto-dolomite indeed precipitates

425 on the edges of illite (Figs. 4A-C).

426 Therefore, we speculate that Ca and Mg ions are favorably adsorbed by

427 electrostatic force onto clay surfaces, forming metal-hydroxyl complex and shedding

428 partial water molecules simultaneously (Fig. 7). In a similar manner to metal-carboxyl,

429 metal-hydroxyl might lower the energy required for carbonation, leaving illite or

430 montmorillonite as a nucleation center for proto-dolomite crystallization, resulting in

431 the formation of a thin dolomite layer (Fig. 7). Once this dolomite layer is created, it is

432 generally thought that the homoepitactic growth of these pre-existing particles will

433 continue when a supersaturated condition is maintained (Roberts et al., 2013).

434 **4.2. Morphological features of low-temperature (proto-)dolomite**

435 It has been repeatedly reported that dumbbell, cauliflower and spherical

436 morphologies of non-stoichiometric dolomite form in microbial laboratory experiments

437 (e.g., Warthmann et al., 2000; van Lith et al., 2003; Bontognali et al., 2008; Sánchez-

438 Román et al., 2008; Qiu et al., 2017). These biogenic dolomites vary in size from

439 several micrometers to a few hundred nanometers and normally consist of numerous

440 nanoglobules (Bontognali et al., 2008; Sánchez-Román et al., 2008). Such

441 morphological and textural features are different from dolomite rhombs synthesized at

442 high temperatures, and therefore have been proposed as potential biosignatures to trace

443 microbial activities in the geological record (Warthmann et al., 2000; Sánchez-Román

444 et al., 2008). However, the morphology and size of proto-dolomite precipitated with the

445 aid of clay minerals are similar to those of microbially-mediated ones. These

446 observations suggest that morphology criteria alone may not unambiguously unravel

447 the biogenic origin of dolomite crystals in sedimentary samples, especially those

448 intergrown with clay minerals. Instead of constituting evidence for its origin, such

449 dumbbell-like or spherical dolomite might be an inherent feature of non-stoichiometric

450 proto-dolomite. Indeed, the same observations were also found in abiotic synthesis of

451 proto-dolomite at 60 °C (e.g., Malone et al., 1996; Rodriguez-Blanco et al., 2015).

452 Furthermore, Rodriguez-Blanco et al. (2015) demonstrated that amorphous Mg-Ca

453 carbonate nanospheres first precipitated and then tended to be coalesced into micro-

454 sized proto-dolomite spheroids, implying that proto-dolomite grows via oriented

455 attachment of primary nanoparticles (De Yoreo et al., 2015) and thus exhibits a

456 nanogranular texture.

457 **4.3. Geological implications**

458   Clay minerals are the most abundant minerals on the Earth's surface (Chamley,

459 1989; Vorhies and Gaines, 2009), and they can be either formed authigenicly or

460 transported into marine waters or lakes by river, air or volcanic eruptions (Chamley,

461 1989). As such, clay minerals should be commonly found in modern dolomite-forming

462 environments. Indeed, it has been repeatedly reported that clay minerals commonly

463 occur in sediments of coastal sabkhas and inland saline lakes in which primary dolomite

464 deposits have emerged, such as the coastal sabkha in Abu Dhabi (UAE) (Sadooni et al.,

465 2010) and highly alkaline playa lakes such as Deep Springs Lake in USA (Meister et

466 al., 2011). Surveys of dolomite authigenesis in these settings also revealed that crystals

467 of dolomite often grow in pore spaces around detrital clay particles (e.g., Sadooni et al.,

468 2010). It is notable that in microbial mats of coastal sabkhas (UAE and Qatar), dolomite

469 crystals were also found associated with authigenic clay minerals (Bontognali et al.,

470 2010; Brauchli et al., 2016). These observations suggest that clay minerals might play

471 a positive role in dolomite crystallization.

472   Our experiments show evidence that illite, montmorillionite and probable other

473 negatively-charged clay minerals in an oversaturated solution could severe as

474 nucleation centers for dolomite. Compared to modern seawater with ca. 0.27 mM CO_3^{2-},

475 higher concentrations of CO_3^{2-} ions (20 mM) used in our precipitation experiments,

476 which correspond to higher saturation state for dolomite. Nevertheless, these

477 parameters are still within the range of values estimated in some environments showing

478 ongoing dolomite authigeneisis and perhaps in ancient sea. For instance, the

479 concentration of CO_3^{2-} of hypersaline dolomitic lakes in the Coorong region (Australia)

480 fluctuates from 0.48 to 24.25 mM, depending on the stage of evaporation (Wright and

481 Wacey, 2005). Moreover, apart from Carboniferous to Permian, it has been suggested

482 that the saturation state of dolomite in ancient seas throughout the Phanerozoic was

483 high compared to the present-day (Riding and Liang, 2005). Under aforementioned

22

484   highly oversaturated conditions, swelling clay minerals (e.g., montmorillionite) that can

485   stay buoyant for longer than non-swelling clays (e.g., illite) can function as a template

486   for the direct precipitation of proto-dolomite from solutions. Once deposited into

487   sediments, negatively-charged clays including swelling and non-swelling phases still

488   have such potential to facilitate dolomite formation. Specifically, it has been well

489   documented that organic matter in marine sediments is tightly associated with clay

490   minerals (Kennedy et al., 2002) and potentially promote the formation of authigenic

491   clays (Bontognali et al., 2014b). Under decomposition of organic matter, NH_3 and CO_2

492   gas would be produced, which diffuse into porewaters and then significantly increase

493   solution pH, carbonate alkalinity and saturation state with respect to dolomite. Clay

494   minerals, together with other negatively-charged compounds (e.g., microorganisms and

495   carboxyl-rich organic matters), could contribute to the crystallization of dolomite. Once

496   these newly-formed dolomites are formed, they might be nuclei for later, more

497   pervasive dolomite formation (Burns et al., 2000; Mazzullo, 2000). Such model might

498   account for the occurrence of dolomite beds associated with organic carbon-rich deep-

499   sea clayey sediments (Meister et al., 2007, 2008).

500   Upon burial diagenesis, proto-dolomite tends to transform into more

501   stoichiometric dolomite through a dissolution-reprecipitation process (Malone et al.,

502   1996; Warren, 2000; Vasconcelos and McKenzie, 1997; Rodriguez-Blanco et al., 2015).

503   Therefore, the clay mineral-catalyzed dolomite precipitation model offers one

504   possibility for interpreting the dolomite formation in certain geological environments,

505 in which a close relationship between clays and dolomite is observed (e.g., Wanas and

506 Sallam, 2016).

507

5. CONCLUSIONS

509   We demonstrate that high negatively-charged clay minerals such as illite and

510 montmorillonite are capable of mediating the formation of proto-dolomite through a

511 metal-chelation mechanism. Cauliflower-like and dumbbell-shaped dolomite crystals

512 are mainly distributed on the edge surface of illite particles, while spheroidal dolomites

513 are observed in montmorillonite-amended systems. The proto-dolomite neoformations

514 display granular textures that consist of nanoscopic particles, morphologically similar

515 to those formed by biotic process. This new data provides laboratory evidence for the

516 catalytic role of clay minerals in dolomite formation and suggests that morphology

517 alone cannot be used as a criterion determining the origin for dolomite in the rock

518 records.

519

24

Associate Editor Frank McDermott and three anonymous reviewers whose comments

improved the quality of this manuscript.

REFERENCES

Arvidson R. S. and Mackenzie F.T. (1999) The dolomite problem: control of precipitation kinetics by temperature and saturation state. *Am. J. Sci.*, **299**, 257-288.

Baker P. A. and Kastner M. (1981) Constraints on the formation of sedimentary dolomite. *Science*, **213**, 214-216.

Balci N. and Demirel C. (2016) Formation of carbonate nanoglobules by a mixed natural culture under hypersaline conditions. *Minerals*, **6**, 122.

Bischoff W. D., Bishop F. C. and Mackenzie F.T. (1983) Biogenically produced magnesian calcite: inhomogeneities in chemical and physical properties; comparison with synthetic phases. *Am. Mineral.*, **68**, 1183-1188.

Bontognali T. R. R., Vasconcelos C., Warthmann R. J., Dupraz C., Bernasconi S. M. and McKenzie J. A. (2008) Microbes produce nanobacteria-like structures, avoiding cell entombment. *Geology*, **36**, 663-666.

Bontognali T. R. R., Vasconcelos C., Warthmann R. J., Bernasconi S. M., Dupraz C., Stohmenger C. J. and McKenzie J. A. (2010) Dolomite formation within microbial mats in the coastal sabkha of Abu Dhabi (United Arab Emirates). *Sedimentology*, **57**, 824-844.

Bontognali T. R. R., Vasconcelos C., Warthmann R. J., Lundberg R. and McKenzie J.

548   A. (2012) Dolomite-mediating bacterium isolated from the sabkha of Abu

549   Dhabi (UAE). *Terra Nova*, **24**, 248-254.

550 Bontognali T. R. R., McKenzie J. A., Warthmann R. J., Vasconcelos C. (2014a)

551   Microbially influenced formation of Mg-calcite and Ca-dolomite in the

552   presence of exopolymeric substances produced by sulphate-reducing bacteria.

553   *Terra Nova*, **26**, 72-77.

554 Bontognali T. R. R., Martinez-Ruiz F., McKenzie J. A., Bahniuk A., Anjos S. and

555   Vasconcelos C. (2014b) Smectite synthesis at low temperature and neutral pH

556   in the presence of succinic acid. *Applied Clay Science*, **101**, 553-557.

557 Botha G. A. and Hughes J. C. (1992) Pedogenic palygorskite and dolomite in a late

558   Neogene sedimentary succession, northwestern Transvaal, South Africa.

559   *Geoderma*, **53**, 139-154.

560 Brauchli M., McKezie J . A., Strohmenger C. J., Sadooni F., Vasconcelos C. and

561   Bontognali T. R. R. (2016) The importance of microbial mats for dolomite

562   formation in the Dohat Faishakh sabkha, Qatar. *Carbonate. Evaporite.*, **31**, 339-

563   345.

564 Budd D. A. (1997) Genozoic dolomites of carbonate islands: their attributes and origin.

565   *Earth-Sci. Rev.*, **42**, 1-47.

566 Burns S. J., McKenzie J. A. and Vasconcelos C. (2000) Dolomite formation and

567   biogeochemical cycles in the Phanerozoic. *Sedimentology*, **47**, 49-61.

568 Capo R. C., Whipkey C. E., Blachère J. R. and Chadwick O. A. (2000) Pedogenic origin

569   of dolomite in a basaltic weathering profile, Kohala peninsula, Hawaii. *Geology*,

570   **28**, 271-274.

571   Casado A. I., Alonso-Zarza A. M. and La lglesia, Á. (2014) Morphology and origin of

572   dolomite in paleosols and lacustrine sequences. Examples from the Miocene of

573   the Madrid Basin. *Sediment. Geol.*, **312**, 50-62.

574   Chamley H. (1989) Clay sedimentology: New York, *Springer-Verlag Berlin Heidelberg*,

575   p. 163-190.

576   Cuadros J., Diaz-Hernandez J. L., Sanchez-Navas A., Garcia-Casco A. and Yepes J.

577   (2016) Chemical and textural controls on the formation of sepiolite,

578   palygorskite and dolomite in vocanic soils. *Geoderma*, **271**, 99-114.

579   de Leeuw N. H. and Parker, S. C. (2001) Surface-water interactions in the dolomite

580   problem. *Phys. Chem. Chem. Phys.*, **3**, 3217-3221.

581   Deng S., Dong H., Lv G., Jiang H., Yu B. and Bishop M.E. (2010) Microbial dolomite

582   precipitation using sulfate reducing and halophilic bacteria: Results from

583   Qinghai Lake, Tibetan Plateau, NW China. *Chem. Geol.*, **278**, 151-159.

584   De Yoreo J. J. and Dove, P. M. (2004) Shaping crystals with biomolecules. *Science*,

585   **306**, 1301-1302.

586   De Yoreo J. J., Gilbert P. U. P. A., Sommerdijk N. A. J. M., Lee Penn R., Whitelam S.,

587   Joester D., Zhang H., Rimer J. D., Navrotsky A., Banfield J. F., Wallace A. F.,

588   Marc Michel F., Meldrum F. C., Cölfen H. and Dove P. M. (2015)

589   Crystallization by particle attachment in synthetic, biogenic and geological

590   environments. *Science*, **349** aaa6760.

591   Diaz-Hernandez J. L., Sámchez-Navas A., Delgado A., Yepes J. and Garcia-Casco A.

592   (2018) Textural and isotopic evidence for Ca-Mg carbonate pedogenesis. *Geochim. Cosmochim. Acta*, **222**, 485-507.

593

594   Disi Z. A. A., Jaous S., Bontognali T. R. R., Attia E. S. M., Al-Kuwari H. A. A. S. and

595   Zouari N. (2017) Evidence of a role for aerobic bacteria in high magnesium

596   carbonate formation in the evaporitic environment of Dohat Faishakh Sabkha

597   in Qatar. *Front. Envrion. Sci.*, **5**, 1.

598   Dogan A. U., Dogan M., Onal M., Sarikaya Y., Aburub A. and Wurster D. E. (2006)

599   Baseline studies of the clay minerals society source clays: Specific surface area

600   by the Brunauer Emmett Teller (BET) method. *Clay Clay Miner.*, **54**, 62-66.

601   Dogan M., Dogan A. U., Yesilyurt F. I., Alaygut D., Buckner I. and Wurster D. E. (2007)

602   Baseline studies of the clay minerals society special clays: Specific surface area

603   by the Brunauer Emmett Teller (BET) method. *Clay Clay Miner.*, **55**, 534-541.

604   Falini G., Gazzano M., Ripamoniti A. (1996) Magnesium calcite crystallization from

605   water-alcohol mixtures. *Chem. Commun.*, 1037-1038.

606   Given R. K. and Wilkinson B.H. (1987) Dolomite abundance and stratigraphic age:

607   constraints on rates and mechanisms of Phanerozoic dolostone formation:

608   Perspectives. *J. Sediment. Petrol.*, **57**, 1068-1078.

609   González-Muñoz M. T., Rodriguez-Navarro C., Martínez-Ruiz F., Arias J. M., Merroun

610   M. L. and Rodriguez-Gallego M. (2010) Bacterial biomineralization: new

611   insights from *Myxococcus*-induced mineral precipitation. *Geol. Soc. London Sp.*

612   *Pub.*, **336**, 31-50.

613   Graf D. L. and Goldsmith J. R. (1956) Some hydrothermal syntheses of dolomite and

614   protodolomite. *J. Geol.*, **64**, 173-186.

615   Gregg J. M., Howard S. A. and Mazzullo S. J. (1992) Early diagenetic recrystallization

616   of Holocene (<3000 years old) peritidal dolomites, Ambergris Cay, Belize.

617   *Sedimentology*, **39**, 143-160.

618   Gregg J. M., Bish D. L., Kaczmarek S. E. and Machel H. G. (2015) Mineralogy,

619   nucleation and growth of dolomite in the laboratory and sedimentary

620   environment: a review. *Sedimentology*, **62**, 1749-1769.

621   Hamm L. M., Wallace A. F., Dove P. M. (2010) Molecular dynamics of ion hydration

622   in the presence of small carboxylated molecules and implications for

623   calcification. *J. Phys. Chem. B* **114**, 10488-10495.

624   Han N., Blue C. R., De Yoreo J. J., Dove P. M. (2013) The effect of carboxylates on the

625   Mg content of calcites that transform from ACC. *Procedia Earth Planet. Sci.*, **7**,

626   223-227.

627   Hatfield C. B. and Rohrbacker T. J. (1966) Dolomite-insoluble residue relationships in

628   the Ten Mile Creak Dolomite (Middle Devonian) near Toledo, Ohio: Notes. *J.*

629   *Sed. Res.*, **3**, 828-831.

630   Jalilehvand F., Spångberg D., Lindqvist-Reis P., Hermansson K., Persson I. and

631   Sandström M. (2001) Hydration of the calcium ion. An EXAFS, large-angle X-

632   ray scattering, and molecular dynamics simulation study. *J. Am. Chem. Soc.*,

633   **123**, 431-441.

634   Jiao D., King C, Grossfield A., Darden T. A., Ren P. (2006) Simulation of Ca^{2+} and

635   Mg^{2+} solvation using polarizable atomic multipole potential. *J. Phys. Chem. B*,

110, 18553-18559.

Jonas L., Müller T., Dohmen R., Immenhauser A., Putlitz B. (2017) Hydrothermal replacement of biogenic and abiogenic aragonite by Mg-carbonates - Relation between textural control on effective element fluxes and resulting carbonte phase. *Geochim. Cosmochim. Acta*, **196**, 289-306.

Kaczmarek S. E. and Sibley D. F. (2011) On the evolution of dolomite stoichiometry and cation order during high-temperature synthesis experiments: An alternative model for the geochemical evolution of natural dolomites. *Sedment. Geol.*, **240**, 30-40.

Kaczmarek S. E. and Thornton B. P. (2017) The effect of temperature on stoichiometry, cation ordering, and reaction rate in high-temperature dolomitization experiments. *Chem. Geol.*, **468**, 32-41.

Kahle C. (1965) Possible roles of clay minerals in the formation of dolomite. *J. Sed.Petrol.*, **35**, 448-453.

Kelleher I. J. and Redfern S. A. T. (2002) Hydrous calcium magnesium carbonate, a possible precursor to the formation of sedimentary dolomite. *Mol. Simulat.*, **28**, 557-572.

Kennedy M. J., Pevear D. R. and Hill R. J. (2002) Mineral surface control of organic carbon in black shale. *Science*, **295**, 657-660.

Kenward P., Goldstein R., Gonzalez L. and Roberts J. (2009) Precipitation of low-temperature dolomite from an anaerobic microbial consortium: the role of methanogenic Archaea. *Geobiology*, **7**, 556-565.

658 Kenward P. A., Fowle D. A., Goldstein R. H., Ueshima M., González L. A. and Roberts

659   J. A. (2013) Ordered low-temperature dolomite mediated by carboxyl-group

660   density of microbial cell walls. *AAPG Bull.*, **97**, 2113-2125.

661 Krause S., Liebetrau V., Gorb S., Sánchez-Román M., McKenzie J. A. and Treude T.

662   (2012) Microbial nucleation of Mg-rich dolomite in exopolymeric substances

663   under anoxic modern seawater salinity: new insight into an old enigma. *Geology*,

664   **40**, 587-590.

665 Land L. S. (1980) The isotopic and trace element geochemistry of dolomite: the state

666   of the art. In: Zenger, D.H., Dunham, J.B., Ethington, R.L. (Eds.), Concepts and

667   Models of Dolomitization. *Spec. Publ.-SEPM*, **28**, 87-110.

668 Land L. S. (1985) The origin of massive dolomite. *J. Geol. Educ.*, **33**, 112-125.

669 Land L. S. (1998) Failure to precipitate dolomite at 25 °C from dilute solution despite

670   1000-fold oversaturation after 32 years. *Aquat. Geochem.*, **4**, 361-368.

671 Lenders J. J. M., Dey A., Bomans P. H. H., Spielmann J., Hendrix M. M. R. M., de With

672   G., Meldrum F. C., Harder S. and Sommerdijk N. A. J. M. (2012) High-

673   magnesian calcite mesocrystals: A corrdination chemistry approch. *J. Am. Chem.*

674   *Soc.*, **134**, 1367-1373.

675 Lippmann F. (1973) Crystal chemistry of sedimentary carbonate minerals, Sedimentary

676   Carbonate Minerals. *Springer*, pp. 5-96.

677 Lippman F. (1982) Stable and metastable solubility diagrams for the system $CaCO_3$-

678      $MgCO_3$-H_2O at ordinary temperatures. *Bull. Mineral.*, **105**, 273-279.

679 Lumsden D. N. (1974) Relationships among insoluble residue, dolostone and limestone

680 facies. *J. Sedment. Petrol.*, **44**, 450-456.

681 Machel H. G. (2004) Concepts and models of dolomitization: a critial reappraisal. *Geol.*

682 *Soc. London Sp. Pub.*, **235**, 7-63.

683 Malone M. J., Baker P. A. and Burns S. J. (1996) Recrystallization of dolomite: An

684 experimental study from 50-200°C. *Geochim. Cosmochim. Acta*, **60**, 2189-2207.

685 Mazzullo S. J. (2000) Organogenic dolomitization in peritidal to deep-sea sediments. *J.*

686 *Sed. Res.*, **70**, 10-23.

687 McKenzie J. A. and Vasconcelos C. (2009) Dolomite Mountains and the origin of the

688 dolomite rock of which they mainly consist: historical developments and new

689 perspectives. *Sedimentology*, **56**, 205-219.

690 Meister P., Mckenzie J. A., Vasconcelos C., Bernasconi S., Frank M., Gutjahr M. and

691 Schrag, D.P. (2007) Dolomite formation in the dynamic deep biosphere: results

692 from the Peru Matgin. *Sedimentology*, **54**, 1007-1031.

693 Meister P., Bernasconi S. M., Vasconcelos C. and McKenzie J. A. (2008) Sealevel

694 changes diagnetic dolomite formation in hemipelagic sediments of the Peru

695 Margin. *Mar. Geol.*, **252**, 166-173.

696 Meister P., Reyes C., Beaumont W., Rincon M., Collins L., Berelson W., Stott L.,

697 Corsetti F. and Nealson K. H. (2011) Calcium and magnesium-limited dolomite

698 precipitation at Deep Springs Lake, California. *Sedimentology*, **58**,   1810-1830.

699 Middelburg J. J., de Lange G. J. and Kreulen R. (1990) Dolomite formation in anoxic

700 sediments of Kau Bay, Indonesia. *Geology*, **18**, 399-402.

701 Mirsal I. A. and Zankl H. (1985) Some phenomenological aspects of carbonate

geochemistry. The control effect of transition metals. *Geol. Rundsch.*, **74**, 367-377.

Morrow D. W. (1982) Diagenesis 1. Dolomite-Part 1: The chemistry of dolomitization and dolomite precipitation. *Geosci. Can.*, **9**, 5-13.

Parkhursr D. L. and Appelo C. A. J. (1999) User's guide to PHREEQC (Version 2) - A computer program for speciation, batch-reaction, one-dimensional transport, and inverse geochimical calculations. U. S. Geol. Survey. Water-Resources Inverstigations Report 99-4259, 299p.

Pérez A. M., Zarza A. M. A., La lglesia Á, García R. M. (2015) Do magnesian clays play a role in dolomite formation in alkaline envrionments? An example from Castañar Cave, Cáceres (Spain). *Geocaceta*, **57**, 15-18.

Petrash D. A., Bialik O. M., Bontognali T. R. R., Vasconcelos C., Roberts J. A., McKenzie J. A. and Konhauser K. O. (2017) Microbially catalyzed dolomite formation: From near-surface to burial. *Earth-Sci. Rev.*, **171**, 558-582.

Qiu X., Wang H., Yao Y. and Duan Y. (2017) High salinity facilitates dolomite precipitation mediated by *Haloferax volcanii* DS52. *Earth Planet. Sci. Lett.*, **472**, 197-205.

Rivadeneyra M. A. A., Delgado G., Soriano M., Ramos-Cormenzana A. and Delgado R. (2000) Precipitation of carbonates by *Nesterenkonia halobia* in liquid media. *Chemosphere* **41**, 617-624.

Rivadeneyra M. A., Párraga J., Delgado R., Ramos-Cormenzana A. and Delgado G. (2004) Biomineralization of carbonates by *Halobacillus trueperi* in solid and

liquid media with different salinities. *FEMS Microbiol. Ecol.*, 48, 39-46.

Rivadeneyra M. A., Delgado R., Párraga J., Ramos-Cormenzana A., Delgado G. (2006) Precipitation of minerals by 22 species of moderately halophilic bacteria in artificial marine salts media: Influence of salt concentration. *Folia Microbiol.*, **51**, 445-453.

Roberts J. A., Bennett P. C., González L. A., Macpherson G. and Milliken K. L. (2004) Microbial precipitation of dolomite in methanogenic groundwater. *Geology*, **32**, 277-280.

Roberts J. A., Kenward P. A., Fowle D. A., Goldstein R. H., González L. A. and Moore D. S. (2013) Surface chemistry allows for abiotic precipitation of dolomite at low temperature. *Proc. Natl. Acad. Sci.*, **110**, 14540-14545.

Rodriguez-Blanco J. D., Shaw S. and Benning L. G. (2015) A route for the direct crystallization of dolomite. *Am. Mineral.*, **100**, 1172-1181.

Romanek C. S., Jiménez-López C., Navarro A. R., Sánchez-Román M., Sahai N., and Coleman M. (2009) Inorganic synthesis of Fe-Ca-Mg carbonates at low temperature. *Geochim. Cosmochim. Acta*, **73**, 5361-5376.

Riding R. and Liang L. (2005) Seawater chemistry control of marine limestone accumulation over the past 550 mallion years. *Rev. Esp. Micropaleontol.*, **37**, 1-11.

Sadooni F. N., Howari F. and El-Saiy A. (2010) Microbial dolomites from carbonate-evaporite sediments of the coastal sabkha of Abu Dhabi and their exploration implications. *J. Petrol. Geol.*, **33**, 289-298.

746 Sánchez-Román M., Vasconcelos C., Schmid T., Dittrich M., McKenzie J. A., Zenobi

747   R. and Rivadeneyra M. A. (2008) Aerobic microbial dolomite at the nanometer

748   scale: Implications for the geologic record. *Geology*, **36**, 879-882.

749 Sánchez-Román M., McKenzie J. A., Wagener A. D. L. R., Rivadeneyra M. A. and

750   Vasconcelos C. (2009) Presence of sulfate does not inhibit low-temperature

751   dolomite precipitation. *Earth Planet. Sci. Lett.*, **285**, 131-139.

752 Sánchez-Román M., McKenzie J. A., de Luca Rebello Wagener A., Romanek C. S.,

753   Sánchez-Navas A. and Vasconcelos C. (2011a) Experimentally determined

754   biomediated Sr partition coefficient for dolomite: Significance and implication

755   for natural dolomite. *Geochim. Cosmochim. Acta*, **75**, 887-904.

756 Sánchez-Román M., Romanek C. S., Fernández-Remolar D. C., Sánchez-Navas A.,

757   McKenzie J. A., Pibernat R. M. and Vasconcelos C. (2011) Aerobic

758   biomineralization of Mg-rich carbonates: Implications for natural environments.

759   *Chem. Geol.*, **281**, 143-150.

760 Shen Z., Liu Y., Brown P. E., Szlufarska I. and Xu H. (2014) Modeling the effect of

761   dissolved hydrogen sulfide on Mg^{2+}-water complex on dolomite {104} surfaces.

762   *J. Phys. Chem. C*, **118**, 15716-15722.

763 Shen Z., Brown P. E., Szlufarska I. and Xu H. (2015) Investigation of the role of

764   polysaccharide in the dolomite growth at low temperature by using atomistic

765   simulations. *Langmuir*, **31**, 10435-10442.

766 Sibley D. F., Dedoes R. E. and Bartlett T. R. (1987) Kinetics of dolomitization. *Geology*,

767   **15**, 1112-1114.

768 Sibley D. F., Nordeng S. H. and Barkowski M.L. (1994) Dolomitization kinetics in

769   hydrothermal bombs and natural settings. *J. Sed. Res.*, **64**, 630-637.

770 Stephenson A. E., De Yoreo J. J., Wu L., Wu K. J. and Dove P. M. (2008) Peptides

771   enhance magnesium signature in calcite: Insights into origins of vital effects.

772   *Science*, **322**, 724-727.

773 van Lith Y., Vasconcelos C., Warthmann R., Martins J. and McKenzie J. (2002)

774   Bacterial sulfate reduction and salinity: two controls on dolomite precipitation

775   in Lagoa Vermelha and Brejo do Espinho (Brazil). *Hydrobiologia*, **485**, 35-49.

776 van Lith Y., Warthmann R., Vasconcelos C. and Mckenzie J. A. (2003) Sulphate-

777   reducing bacteria induce low-temperature Ca-dolomite and high Mg-calcite

778   formation. *Geobiology*, **1**, 71-79.

779 Vasconcelos C., McKenzie J. A., Bernasconi S., Grujic D. and Tiens A. J. (1995)

780   Microbial mediation as a possible mechanism for natural dolomite formation at

781   low temperatures. *Nature*, **377**, 220-222.

782 Vasconcelos C. and McKenzie J. A. (1997) Microbial mediation of modern dolomite

783   precipitation and diagenesis under anoxic conditions (Lagoa Vermelha, Rio de

784   Janeiro, Brazil). *J. Sed. Res.*, 67, 378-390.

785 Vorhies J. S. and Gaines R. R. (2009) Microbial dissolution of clay minerals as a source

786   of iron and silica in marine sediments. *Nat. Geosci.*, **2**, 221-225.

787 Wanas H. A. and Sallam, E. (2016) Abiotically-formed, primary dolomite in the mid-

788   Eocene lacustrine succession at Gebel El-Goza El-Hamra, NE Egypt: An

789   approach to the role of smectitic clays. *Sediment. Geol.*, **343**, 132-140.

790   Wang D., Wallace A. F., De Yoreo J. J. and Dove P. M. (2009) Carboxylated molecules

791   regulate magnesium content of amorphous calcium carbonates during

792   calcification. *Proc. Natl. Acad. Sci.*, **106**, 21511-21516.

793   Warren J. (2000) Dolomite: occurrence, evolution and economically important

794   associations. *Earth-Sci. Rev.*, **52**, 1-81.

795   Warthmann R., van Lith Y., Vasconcelos C., McKenzie J. A. and Karpoff A. M. (2000)

796   Bacterially induced dolomite precipitation in anoxic culture experiments.

797   *Geology*, **28**, 1091-1094.

798   Wells A. J. (1062) Recent dolomite in the Persian Gulf. *Nature*, **194**, 274-275.

799   Wright D. T. (1999) The role of sulphate-reducing bacteria and cyanobacteria in

800   dolomite formation in distal ephemeral lakes of the Coorong region, South

801   Australia. *Sediment. Geol.*, **126**, 147-157.

802   Wright D. T. and Wacey D. (2005) Precipitation of dolomite using sulphate-reducing

803   bacteria from the Coorong Region, South Australia: significance and

804   implications. *Sedimentology*, **52**, 987-1008.

805   Zhang F., Xu H., Konishi H., Shelobolina E. S. and Roden E. (2012a) Polysaccharide-

806   catalyzed nucleation and growth of disordered dolomite: A potential precursor

807   of sedimentary dolomite. *Am. Mineral.*, **97**, 556-567.

808   Zhang F., Xu H., Konishi H., Kemp J. M., Roden E. E. and Shen, Z. (2012b) Dissolved

809   sulfide-catalyzed precipitation of disordered dolomite: Implications for the

810   formation mechanism of sedimentary dolomite. *Geochim. Cosmochim. Acta*, **97**,

811   148-165.

812   Zhang F., Xu H., Shelobolina E. S., Konishi H., Converse B., Shen Z. and Roden E. E.

813   (2015) The catalytic effect of bound extracellular polymeric substances excreted

814   by anaerobic microorganisms on Ca-Mg carbonate precipitation: Implications

815   for the "dolomite problem". *Am. Mineral.*, **100**, 483-494.

816

817 **Table 1**

818 Types of clay minerals used in this study, their surface area, chemical composition and mineralogy.

Minerals	BET surface area (m²/g)	Chemical formula	Mineralogy
Illite (IMt-1)	20.5^a	$(Mg_{0.09}Ca_{0.06}K_{1.37})(Al_{2.69}Fe_{0.82}Mg_{0.43}Ti_{0.06})(Si_{6.77}Al_{1.23})O_{20}(OH)_4$ [b]	Illite, trace quartz
Montmorillonite (SWy-2)	22.7^c	$(Ca_{0.12}Na_{0.32}K_{0.05})(Al_{3.01}Fe_{0.41}Mn_{0.01}Mg_{0.54}Ti_{0.02})(Si_{7.98}Al_{0.02})O_{20}(OH)_4$ [b]	Montmorillonite, trace quartz,
Kaolinite (KGa-1b)	13.1^c	$(Mg_{0.02}Ca_{0.01}Na_{0.01}K_{0.01})(Al_{3.86}Fe_{0.02}Ti_{0.11})(Si_{3.83}Al_{0.17})O_{10}(OH)_8$ [b]	Kaolinite

819   [a] Dogan et al. (2007).   [b] http://www.clays.org/Sourceclays.html.   [c] Dogan et al. (2006).

820

821

822

823 **Table 2**

824 Geochemical changes in the carbonation reactors with and without clay mineral (6 g/L).

825

Experimental set	Initial pH	Initial Ca^{2+} (mM)	Initial Mg^{2+} (mM)	Initial SI for carbonate phases				Final pH	Final Ca^{2+} (mM)	Final Mg^{2+} (mM)
				calcite	aragonite	monohydrocalcite	proto-dolomite			
Without clay mineral	9.74	9.91	81.03	4.77	4.65	3.44	10.02	9.01	0.92	80.89
With illite	9.78	9.95	80.47	4.78	4.66	3.45	10.03	9.09	1.05	72.32
With montmorillonite	9.79	10.07	80.26	4.79	4.67	3.46	10.03	9.11	0.98	76.67
With kaolinite	9.71	10.02	80.14	4.78	4.67	3.45	10.03	9.03	0.84	79.56

Figure caption:

Figure 1. XRD patterns of minerals obtained before and after carbonation experiments: (A) mineral products without clay additives; (B) pristine illite IMt-1; (C) solid products with IMt-1 as the additive; (D) standards of proto-dolomite, ordered-dolomite and hydromagnesite (A, aragonite; I, illite; Q, quartz; D, dolomite).

Figure 2. XRD patterns for the solid samples collected before and after carbonation experiments: (A) original montmorillonite SWy-2; (B) neoformed crystals with SWy-2; (C) pristine kaolinite KGa-1b; (D) solid phases with KGa-1b (M, montmorillonite; Q, quartz; D, dolomite; A, aragonite; K, kaolinite; MC, monohydrocalcite).

Figure 3. Raman spectra for the solids from the carbonation reactor with 6 g/L IMt-1, pristine IMt-1, and standards of proto-dolomite, ordered-dolomite and hydromagnesite. The arrows and dash lines highlight the characteristic bands of proto-dolomite occurring in carbonation sample with IMt-1 as the additive.

Figure 4. SEM images of proto-dolomite synthesized in the solutions with illite. (A-C) micron-sized dolomites (arrow) on the edge surface of illite; (D-E) the newly-formed proto-dolomites appear as cauliflower and dumbbell grains, respectively; (F) a magnified view that shows the details of neoformed proto-dolomite; (G-J) elemental maps of the association between proto-dolomite and illite showing the distribution of

847   Ca, Mg and Si; (K-L) typical EDS compositions of illite and protodolomite shown in

848   panel G (the Pt peaks correspond to sample coating).

849

850   Figure 5. SEM images of proto-dolomite synthesized in the reactors with

851   montmorillonite. (A) montmorillonite samples after carbonation; (B) enlarged views

852   show spheroidal proto-dolomites surrounded by flaky montmorillonite; (C) EDS

853   spectra showing the elemental compositions of montmorillonite and proto-dolomite

854   neoformation (the Pt signal is attributed to sample coating); (D) a high magnified image

855   of proto-dolomite spheroid (the insert) displaying a granular-textured surface.

856

857   Figure 6. (A) TEM micrograph and EDS compositions showing the spatial association

858   between proto-dolomite and illite particles; (B-C) high-magnification images of the

859   inset views of dumbbell or cauliflower-like crystals indicating that nanocrystallites are

860   at random orientations. The inset SAED pattern with indexation as dolomite does not

861   show the super-lattice reflections; (D) HRTEM image showing the occurrence of

862   0.2906 nm lattice fringes, corresponding to d-spacing of (104).

863

864   Figure 7. Schematic diagram illustrating the catalytic role of negatively-charged clay

865   minerals in proto-dolomite formation: (A) diagrammatic crystal structure of 2:1 layer

866   clay minerals (e.g., illite and montmorillonite tested in this study); (B) the adsorption

867   and dewatering of Mg and Ca ions by surface-bound hydroxyl groups; (C) the formation

868   of Mg(Ca)-hydroxyl complexes favoring the carbonation reaction.
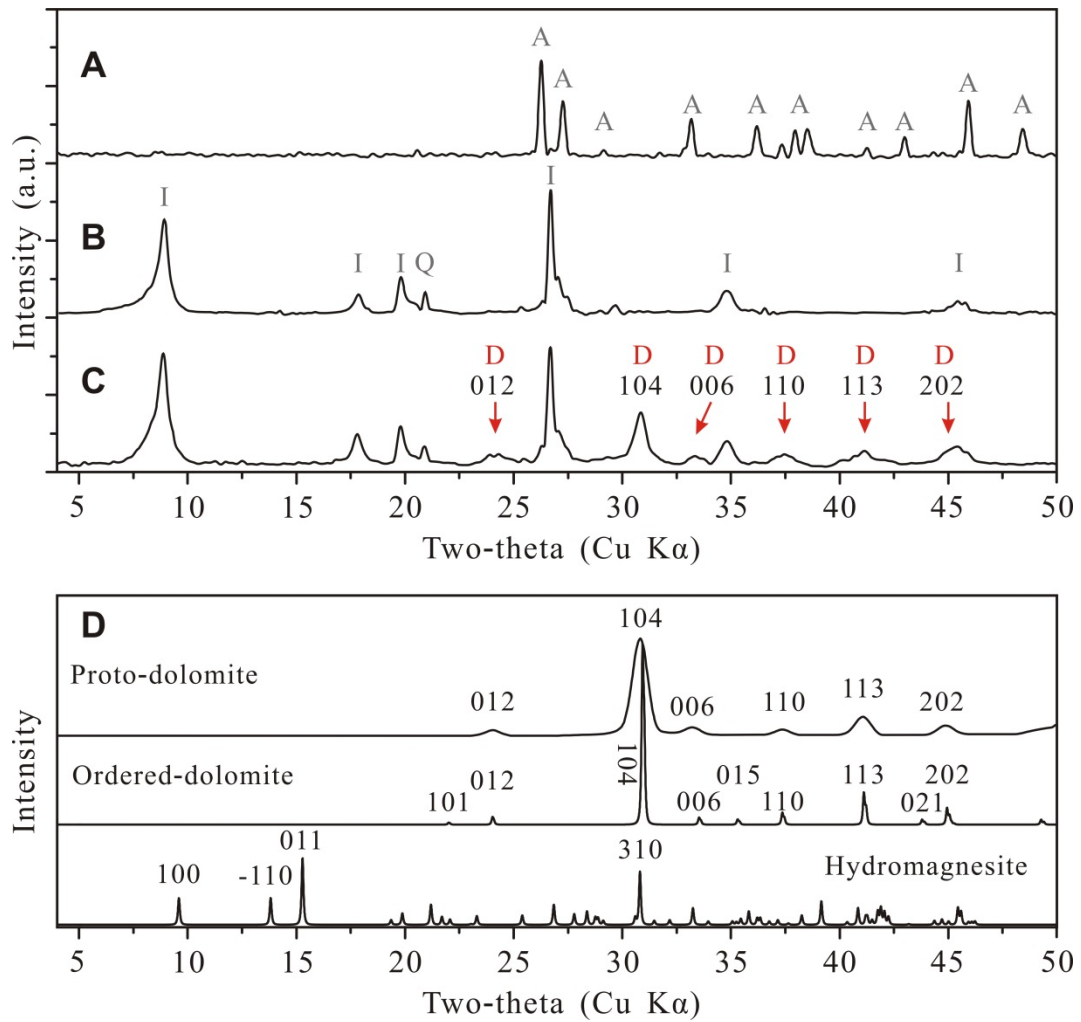
Figure 1
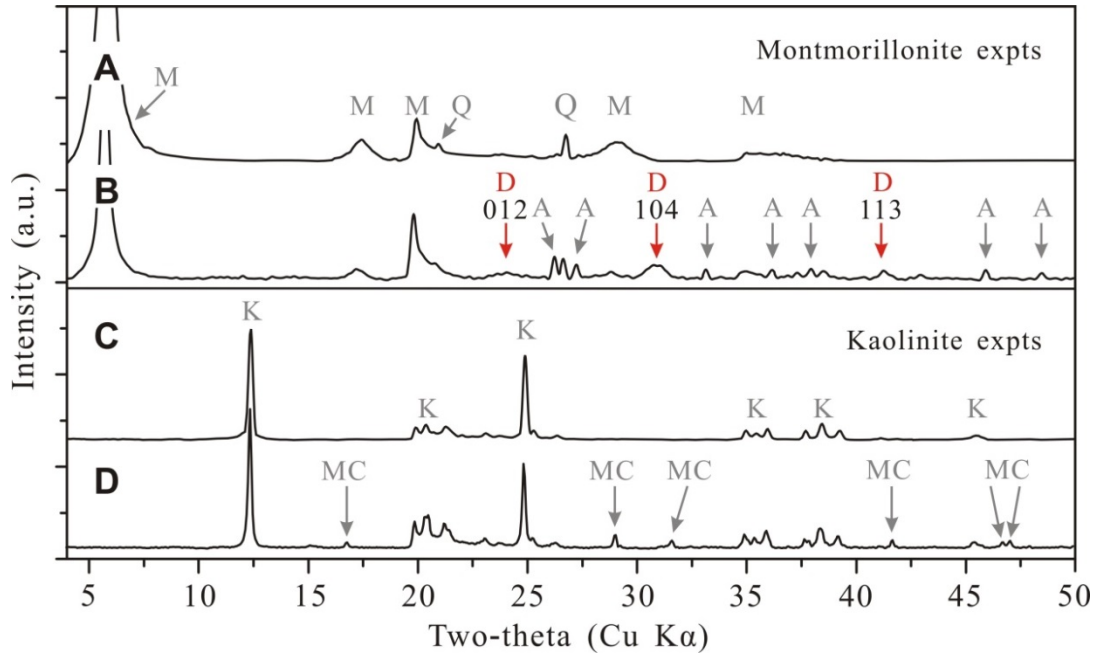
Figure 2
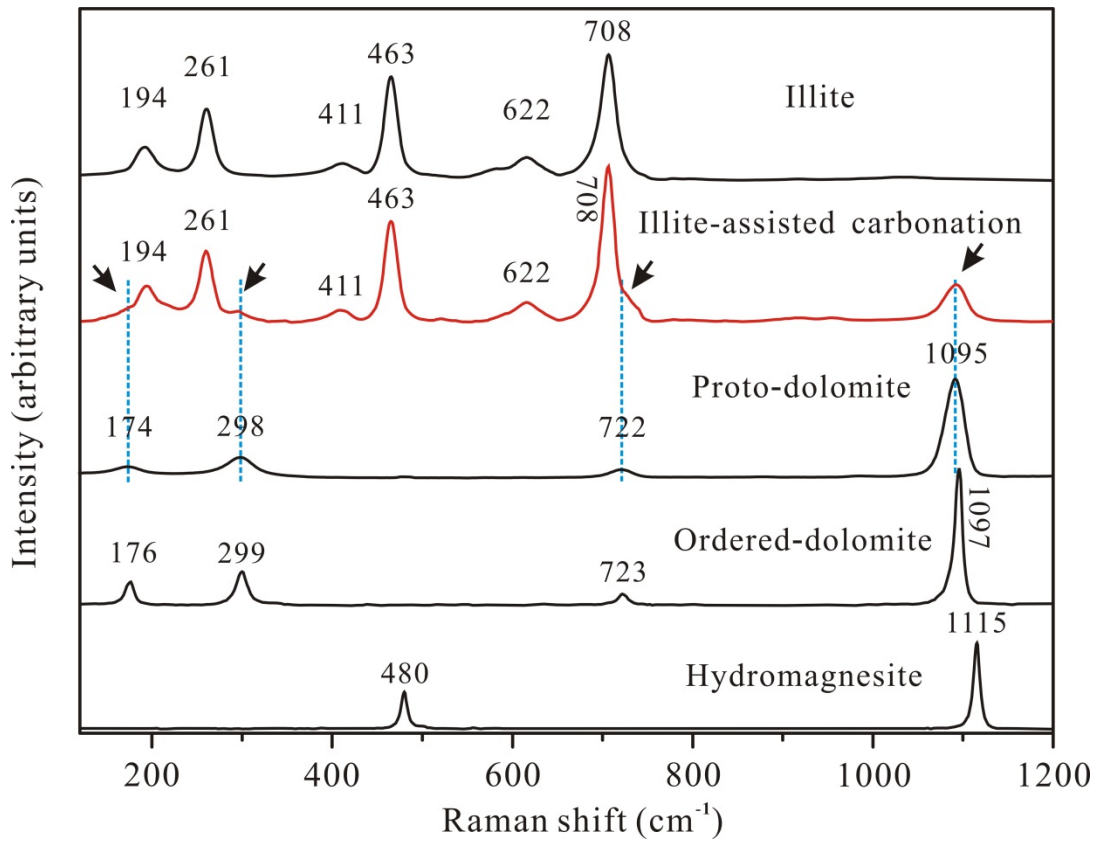
Figure 3
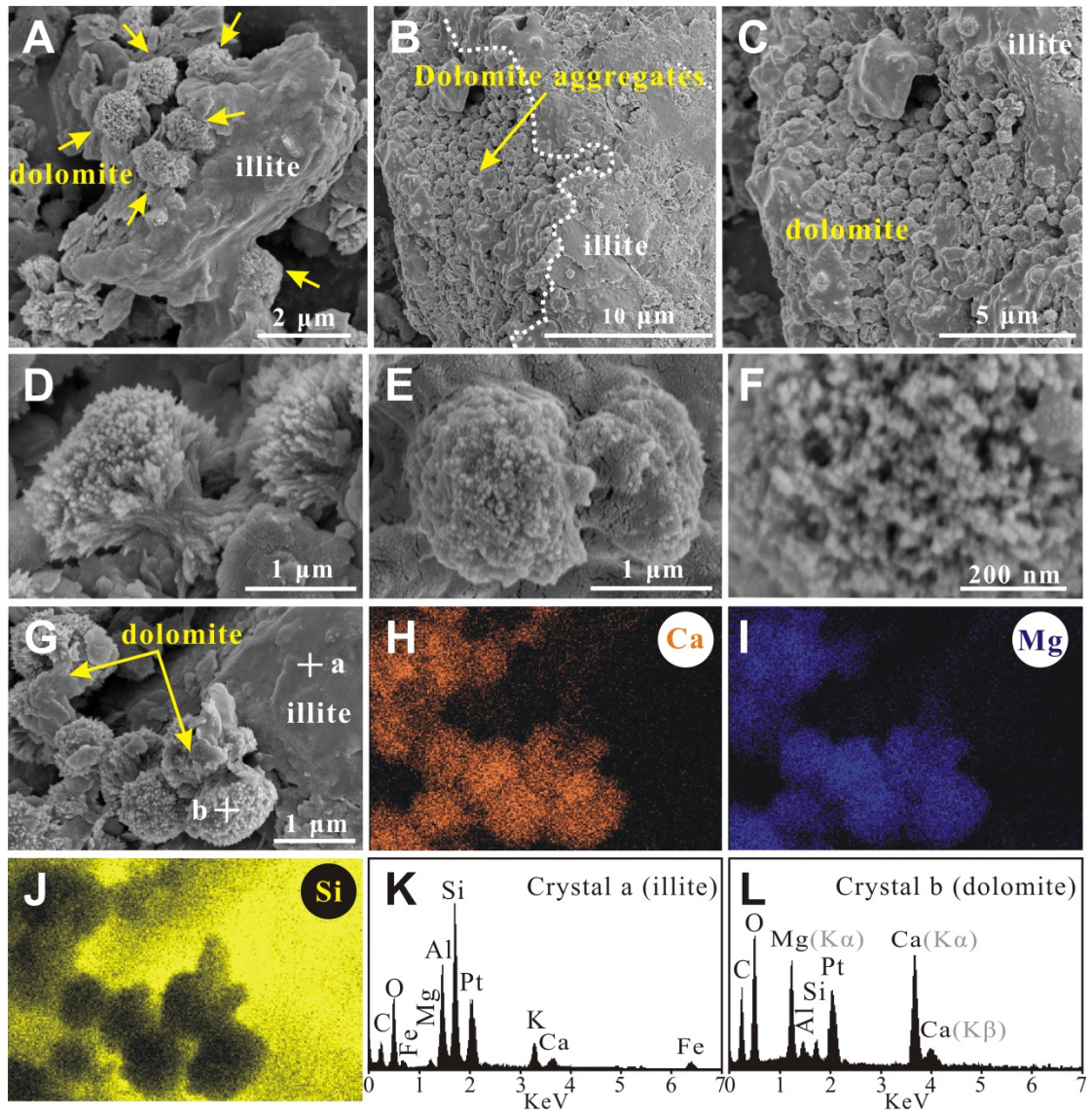
Figure 4
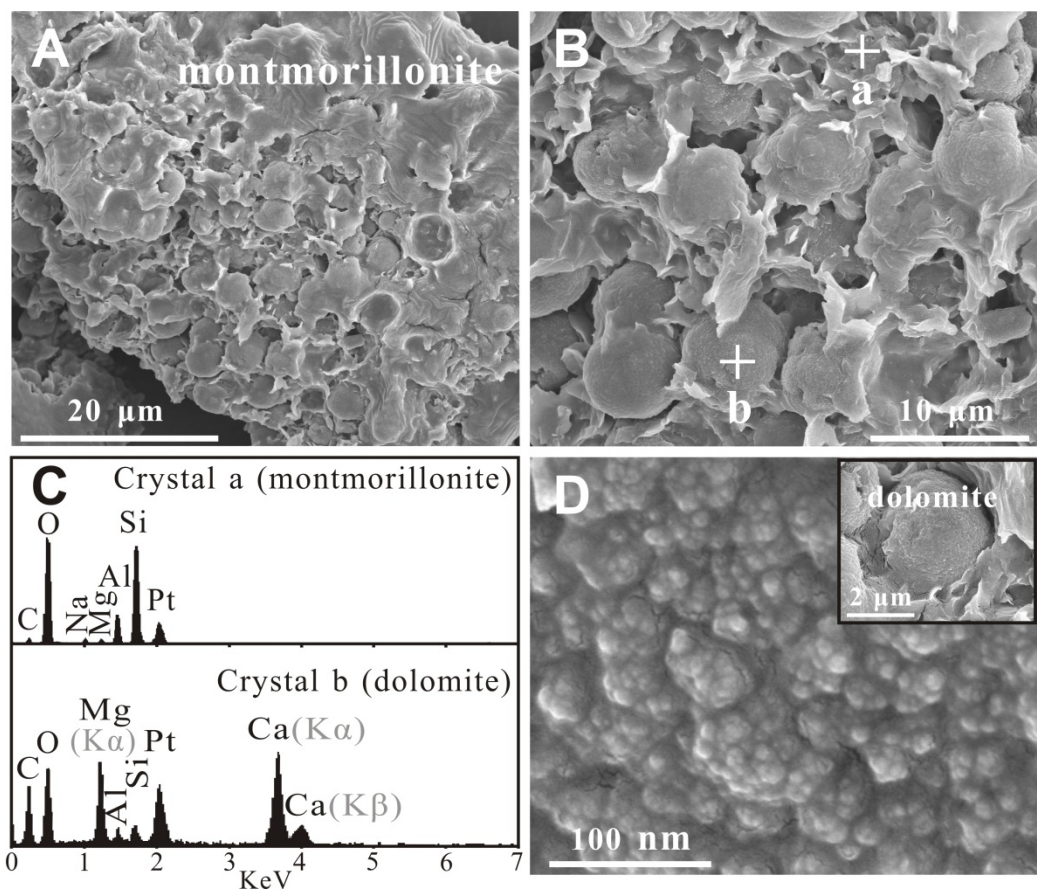
Figure 5
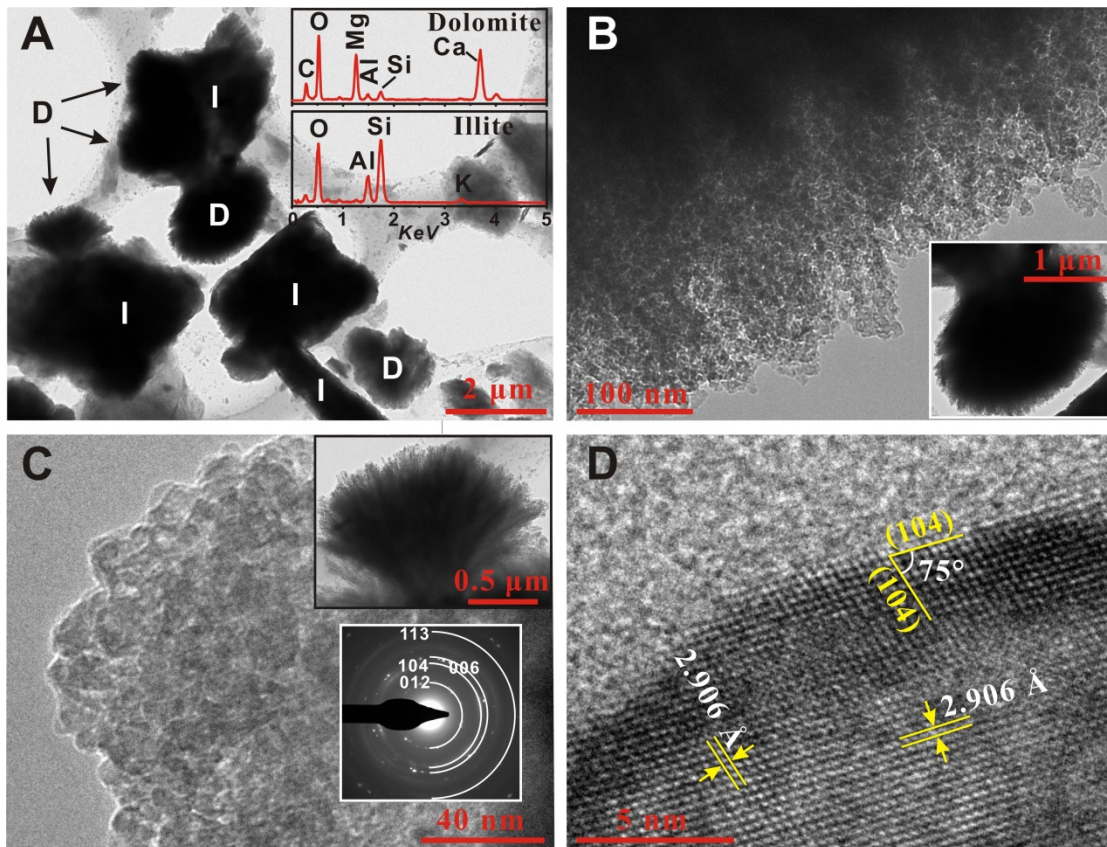
Figure 6
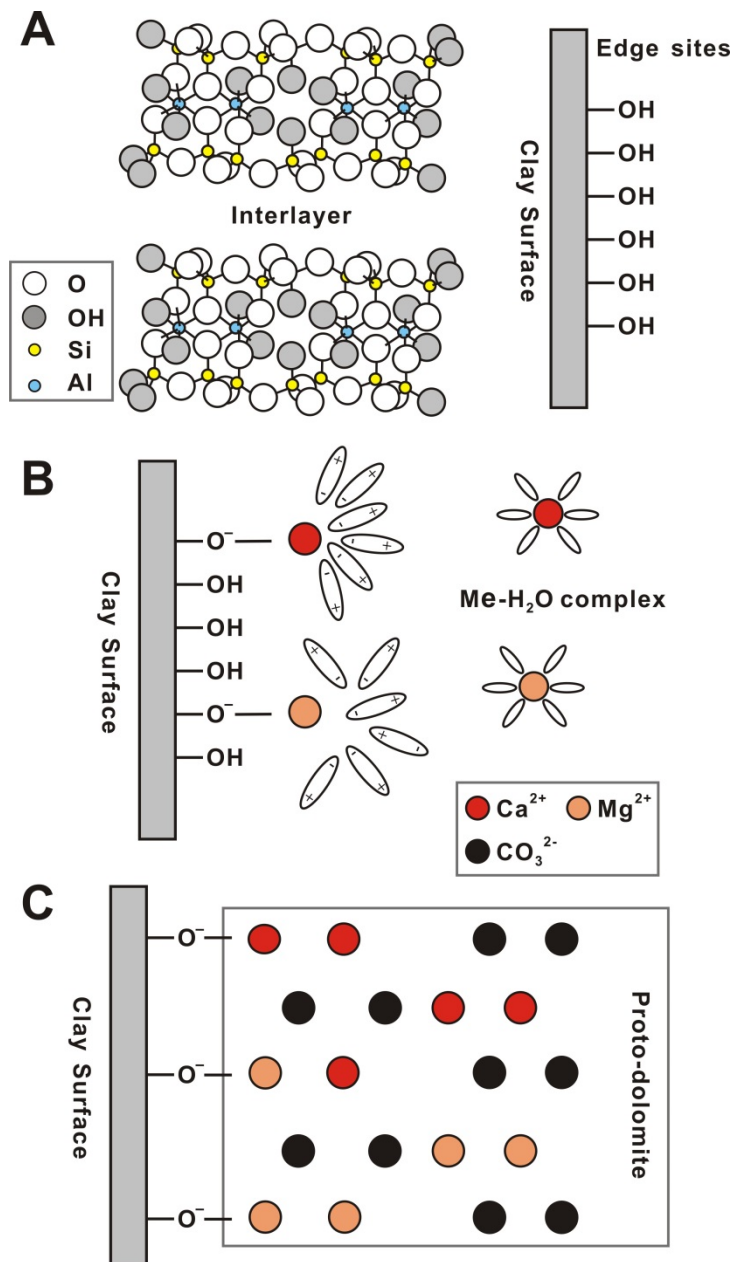
Figure 7

Supplementary material for

Experimental evidence for abiotic formation of low-temperature proto-dolomite

facilitated by clay minerals

Deng Liu[1, 2, *], Yangyang Xu[1], Dominic Papineau[1, 3, 4, 5], Na Yu[2], Qigao Fan[2], Xuan

Qiu[1] and Hongmei Wang[1, 2]

[1]State Key Laboratory of Biogeology and Environmental Geology, China University of

Geosciences, Wuhan 430074, China

[2]School of Environmental Studies, China University of Geosciences, Wuhan 430074,

China

[3]London Centre for nanotechnology, University College London, 17-19 Gordon

Street, London, UK

[4]Department of Earth Sciences, University College London, London, UK

[5]Center for Planetary Sciences, University College London, London, UK

Corresponding authors:

Deng Liu (liud_cug@126.com) and Hongmei Wang (wanghmei04@163.com)

Number of Figures: 4

894 **Figure S1.** TGA analyses of pristine illite and montmorillonite samples.

895
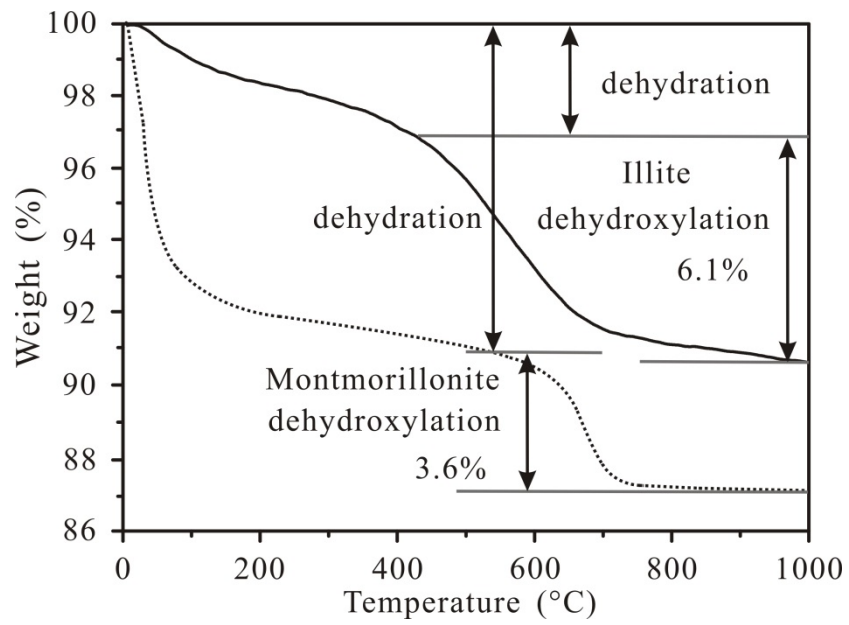
896
897
898
899
900
901
902
903
904
905
906
907
908
909

910 **Figure S2.** XRD patterns for the solid samples collected from the carbonation

911 experiments using different concentrations of illite (I, illite; Q, quartz; D, dolomite; MC,

912 monohydrocalcite; A, aragonite; H, hydromagnesite).

913
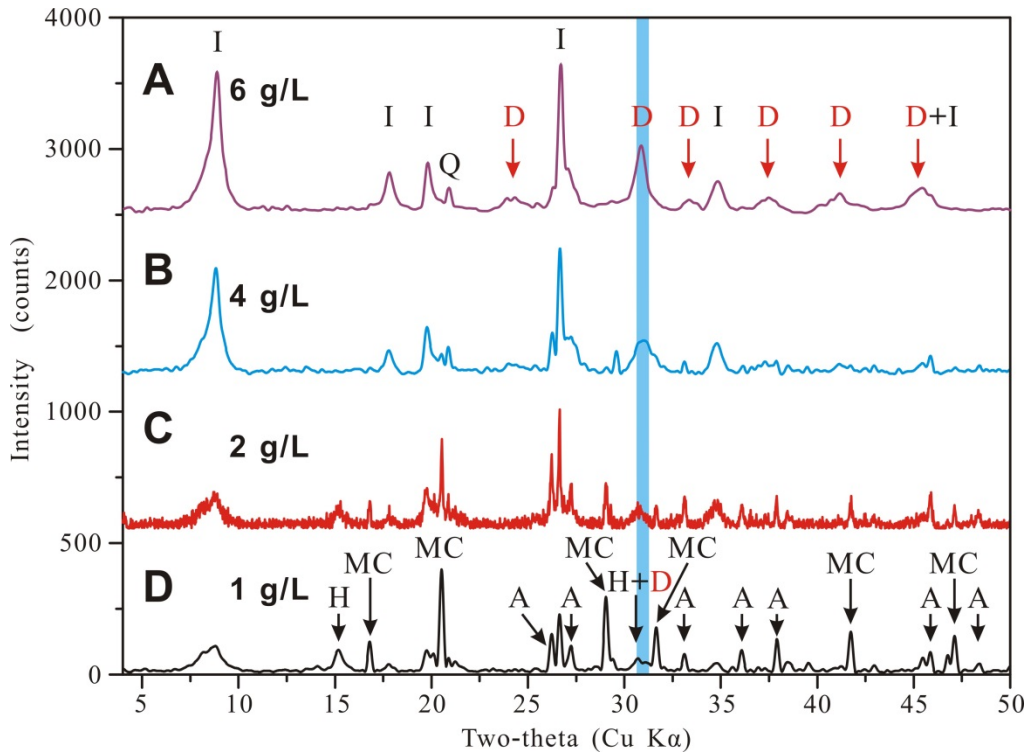
914
915
916
917
918
919
920
921
922
923

Figure S3. XRD patterns for the solid samples collected from the carbonation

experiments using different concentrations of montmorillonite (M, montmorillonite; Q,

quartz; D, dolomite; MC, monohydrocalcite; A, aragonite).

52
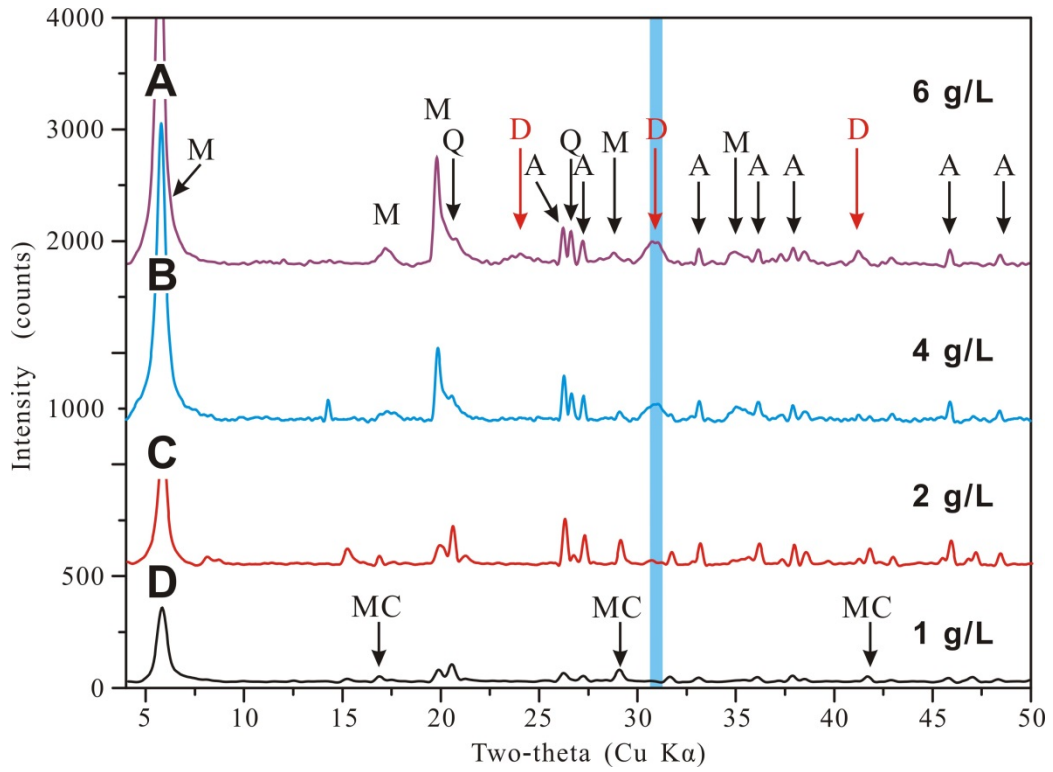
945 **Figure S4.** Result of the SEM-EDS analysis of newly-formed aragonite observed in

946 the systems with montmorillonite. The Pt peak showing in EDS came from sampling

947 coating.

948

949

950